Energy Storage Materials 67 (2024) 103326

Contents lists available at ScienceDirect

Energy Storage Materials

journal homepage: www.elsevier.com/locate/ensm

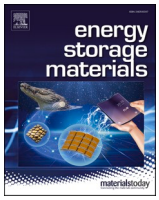

Additive-rejuvenated anions (De)intercalation into graphite cathode enables optimum dual-ion battery

Ying Zheng, Wei Zhang *, Fuxi Liu, Qing Liang, Wenwen Li, Xinyan Zhou, Nailin Yue, Weitao Zheng *

Key Laboratory of Automobile Materials MOE, School of Materials Science & Engineering, Electron Microscopy Center, International Center of Future Science, Jilin Provincial International Cooperation Key Laboratory of High-Efficiency Clean Energy Materials, Jilin University, Changchun 130012, China

ARTICLE INFO

Keywords:
Aqueous electrolyte
Graphite cathode
Dual-ion battery
Cathode electrolyte interphase
$C_3H_3FO_3$

ABSTRACT

Cathode-electrolyte interphase (CEI) has particular function in maintaining electrolyte and cathode stability. However, the CEI will also cause some negative effects on ion transport. It is crucial for optimizing the structure of CEI through additives in the electrolyte to improve the electrode reaction. In this study, we proposed using $C_3H_3FO_3$ (FEC) as an additive to optimize an aqueous LiTFSI (bistrifluoromethanesulfonimide lithium salt) electrolyte. The incorporation of FEC modified the solvation structure of $TFSI^-$, inhibit the formation of CEI with thicker size, thereby facilitating the intercalation of $TFSI^-$ into the selected graphite cathode. Consequently, the graphite's discharge capacity was doubled, reaching 47 mAh g^{-1}. The influence of $TFSI^-$ solvation structure on CEI formation was further studied by the emerging correlative SEM, Raman imaging and TOF-SIMS techniques and theoretical calculation techniques. Using this optimization strategy, we successfully constructed an aqueous dual-ion battery using $C_{24}H_{10}N_2O_4$ and graphite as the anode and cathode with an impressive potential window of 2.55 V, which delivered the energy density of 66 Wh kg^{-1} at the power density of 128 W kg^{-1}.

1. Introduction

The energy density of aqueous rechargeable batteries is severely limited due to the hydrogen/oxygen evolution reaction (HER/OER) of water molecules. In 2015, the water-in-salt (WIS) electrolyte was discovered to overcome the limitation of a narrow electrochemical window and enable the construction of a 2.3 V aqueous Li-ion battery [1]. In a dilute solution, four H_2O molecules reside in the primary sheath of Li^+ [2]. In WIS electrolytes, however, H_2O in the primary sheath is reduced, with $TFSI^-$ participating in solvation, thereby extending the electrochemical window of WIS electrolyte. Various salts, including $NaBF_4$ [3], KCF_3SO_3 [4], $NaClO_4$ [5], $ZnCl_2$ [6], $LiNO_3$ [7], KCH_3COO [8] and $MgCl_2$ [9] are suitable for WIS electrolytes. However, the barriers of high cost and low ion migration rate have impeded the widespread application of these salts. Optimization is typically implemented by i) constructing a localized water-in-salt electrolyte using an inert solvent dissolved in water as a diluent, thereby reducing the electrolyte concentration without destroying the structure of WIS electrolyte [10,11], and by ii) modifying the electrolyte structure with additives [12], thereby changing the carrier's solvation structure, optimizing the interfacial electrochemical reaction, and breaking the hydrogen bond between H_2O to further suppress HER and OER [13]. Wang et al. investigated the performance of tetraethylene glycol diacrylate, ethylene carbonate, and 1,5-pentanediol as diluents in $LiNO_3$ electrolytes, achieving a wide potential window of 2.9 V [14].

However, these studies have primarily focused on the solvation structure of cations and improving the electrolyte's electrochemical window, and the solvation structure of anions—which function as carriers in dual-ion batteries—remains unclear [15–17]. It has been reported that the potential of the graphite cathode in higher concentration electrolyte is positively correlated with the difference between the intercalation energy and solvation energy of anions [3]. More importantly, however, changes in the carrier' solvation structure by additives often induce different solid-electrolyte interphases (SEI) and cathode-electrolyte interface (CEI) at the anode and cathode, respectively [10]. The SEI can be categorized into cationic solvent-derived SEI and anion-derived SEI [18,19]. Generally, anion-derived SEI is advantageous for electrodes in achieving enhanced stability [20]. It has been observed that anions with a cycle structure possess a lower LUMO level compared to those with a point or linear structure, exhibit high electron

* Corresponding author.
E-mail addresses: weizhang@jlu.edu.cn (W. Zhang), wtzheng@jlu.edu.cn (W. Zheng).

https://doi.org/10.1016/j.ensm.2024.103326
Received 4 December 2023; Received in revised form 24 February 2024; Accepted 4 March 2024
Available online 5 March 2024

affinity, and tend to form anion-derived SEI on the anode surface. For instance, the HOMO and LUMO of cyclic $HFDF^-$ ion solvated clusters are predominantly situated in anions, thereby facilitating highly efficient $HFDF^-$ anion-derived SEI and CEI formation [21]. The weakening of the interaction between cations and solvents in the electrolyte, coupled with the strengthening of the interaction between cations and anions, promotes the formation of anion-derived SEI or CEI [22]. Certain high-fluorine solvents [18], 1,2-diethoxyethane and tris (2,2,2-trifluoroethyl) phosphate can disrupt the interaction between cations and solvents, leading to the development of a uniform and thin SEI or CEI [23]. Moreover, the site resistance of solvent molecules can enhance the interaction between anions and cations, thereby inducing the formation of anion-derived SEI or CEI [24]. During the charging process, the cations and anions migrate to the anode and cathode to participate in the electrochemical reaction in a dual-ion battery. Because the anions are enriched on the cathode surface, the solvation structure of the anions will inevitably affect the formation of CEI, modifying the electrode properties. Therefore, it is very important to study the anion's solvation structure and the influence of solvation structure on CEI. Unfortunately, no reports have been found to address such issues.

In this work, we treat FEC as both diluent and additive to achieve a LiTFSI aqueous electrolyte with a lower concentration (3.9375 M, labeled as FEC-added electrolyte). It enables improving the stability of the electrolyte, broaden the potential window, and reduce the cost of WIS electrolyte effectively. In addition, this work fills blank space of research on the optimization of battery properties by anion solvation. Our findings indicated that FEC can reduce the hydrogen bonding density (HBD) in the electrolyte to suppress the transmission of H^+ and OH^-, so that the electrochemical window of the electrolyte is widened. FEC participates in the $TFSI^-$' solvation structure, plays a protective role in $TFSI^-$ ions, and inhibits the decomposition of $TFSI^-$ at high potential to produce CEI with thicker size. The optimized CEI is conducive to the $TFSI^-$ ion from the electrolyte to traverse the CEI to the graphite interlayer to form a graphite intercalation compound (GIC), and then the discharge capacity of graphite cathode is doubled. Ultimately benefited from this anion optimization strategy, graphite cathode was paired with a $C_{24}H_{10}N_2O_4$ (PTCDI, perylenediimide) anode to assemble an aqueous dual-ion battery delivering a potential window of 2.55 V.

2. Results and discussion

2.1. Electrochemical and theoretical calculation characterization of electrolytes

Raman spectroscopy tests on the FEC-added and LiTFSI electrolytes demonstrate that the addition of FEC did not cause new phases to emerge (Fig. S1). Thus, FEC as the additive will not cause a strong chemical reaction to generate new substances and then hinder the electrochemical process of cathode and anode. Contact angle (CA) testing results indicated that FEC reduced the CA of the pristine electrolyte from 33° to 20.8° (Fig. S2). This CA decrease demonstrated the FEC-added electrolyte more easily infiltrated graphite cathode, with favorable wettability enabling increased ionic conduction, reduced interfacial resistance, and enhanced $TFSI^-$-graphite reactivity. The electrochemical impedance test results indicate that the graphite electrode exhibits lower charge transfer resistance (R_{ct}) in the electrolyte with the added FEC (Fig. S3). The equivalent circuit fitting data is presented in Table S1, showing a decrease in solution resistance (R_s) from 1.821 to 1.601 Ω following the addition of FEC. The ionic conductance of the electrolytes can be calculated using Formula 1 [3]:

$$\sigma = \frac{Z'}{Z'^2 + Z''^2} \times \frac{l}{A} \quad (1)$$

where l represents the distance between the positive and negative electrodes, and A represents the electrode area. In this experiment, l and A are 0.8 cm and 1 cm^2, respectively. The ion conductances of the pristine and FEC-added electrolytes are 439 and 500 mS cm^{-1}, respectively. LSV test was carried out to investigate the stability of pristine and FEC-added electrolyte. The results reveal a electrochemical window of 2.6 V for the pristine electrolyte (Fig. 1a), and a weak peak in the range of 0.68 to 1.73 V indicated the decomposition of LiTFSI salts at higher potentials. Upon the addition of FEC to the LiTFSI-based parent electrolyte, the above peak turns to be vanished, rendering the FEC-added electrolyte more stable with an overall potential of approximately 3.6 V. This result shows that FEC, as an additive and diluent, enables broadening the electrochemical window of the electrolyte and enhance the electrolyte's stability. The shift of the electrochemical window of the electrolyte is closely related to the content of free water and the solvation structure of cations/anions. So molecular dynamics calculation was employed to depict the SDF of H_2O molecules in both electrolytes (Fig. 1b and Fig. 1c). In the pristine electrolyte, H_2O easily contacted O in $TFSI^-$ whereas in the FEC-added electrolyte, H_2O preferentially contacted O in FEC. This spatial change causes the structural change of hydrogen bond, as shown in Table 1. The addition of FEC reduces the HBD between water and $TFSI^-$ and new hydrogen bonds were formed between FEC and water molecules. The HBD between the water molecules will also decrease and eventually the total HBD of the electrolyte reduced the HBD from 11.5 to 6.18 nm^{-3}. The reduction of HBD can effectively inhibit the transmission of H^+ and OH^- ions, inhibit the reaction of OER and HER, and broaden the electrochemical window of the electrolyte to 3.6 V in FEC-added electrolyte. The DOS results for both electrolytes are depicted in Fig. 1d and e. In the LiTFSI electrolyte, the DOS at the valence band maximum (VBM) is primarily contributed by the oxygen and fluorine atoms from water and $TFSI^-$. When FEC is introduced into the electrolyte, the peaks associated with oxygen and fluorine atoms near the VBM shift towards lower energy. This implies that the addition of FEC can potentially enhance the stability of electrolyte and inhibited LiTFSI decomposition. According to the RDF of $TFSI^-$ (Fig. 1f), the addition of FEC makes the first peak of Li^+ and water slightly negative shift, proving that the primary solvent sheath structure of $TFSI^-$ in FEC-added electrolyte is more compact. Furthermore, $TFSI^-$' SDF also shows that the distribution of water and Li^+ ions around $TFSI^-$ is loose in pristine electrolyte (Fig. 1g), while the distribution of water and Li^+ is dense in FEC-added electrolyte (Fig. 1h). More interestingly, FEC is more likely to participate in the solvation structure of $TFSI^-$ outside Li^+ and water. The resulting solvated structures are $TFSI_4[Li]_2[H_2O]_4$ and $TFSI_4[Li]_2[H_2O]_4[FEC]_2$ in the LiTFSI and FEC-added electrolytes, respectively. Therefore, adding FEC reduced HBD and changed the $TFSI^-$ solvation structure, enhancing its stability.

In the transport process, $TFSI^-$ exhibited independent movement at 4.35, 4.68, 5.18, 7.03, 8.36 and 11.20 ps (Fig. 2a-f). It may be due to the large volume of $TFSI^-$ ion and the contact between the $TFSI^-$ ions, leading to the instability of the solvation structure. This result suggests that the water molecules in the solvated structure of $TFSI^-$ ions are not transported to the electrode surface together, which reduces the occurrence of OER and HER. In addition, this independence movement makes $TFSI^-$ ions have faster dynamic process. Thus, Li^+ is linked to four oxygen at 4.35 ps and 4.68 ps whereas it is linked to three oxygen at 5.18 ps. Li^+ gains one water molecule and then gradually loses another with constant movement in the FEC-added electrolyte, and Li^+ ion has the jump mechanism ion transport mode. Li^+ and $TFSI^-$ are transmitted in the same way in the pristine electrolyte in Fig. S4.

2.2. Structural and electrochemical characterization of graphite cathode

The purpose of electrolyte optimization is to promote the electrode reaction toward high performance of batteries. Therefore, the influence of FEC on the anion intercalated graphite was investigated. As shown in Fig. 3a, the discharge specific capacity of graphite cathode in the FEC-added electrolyte was 47 mAh g^{-1} at 285 mA g^{-1}, whereas in the LiTFSI electrolyte, it was only 22 mAh g^{-1}. It is obvious that FEC can

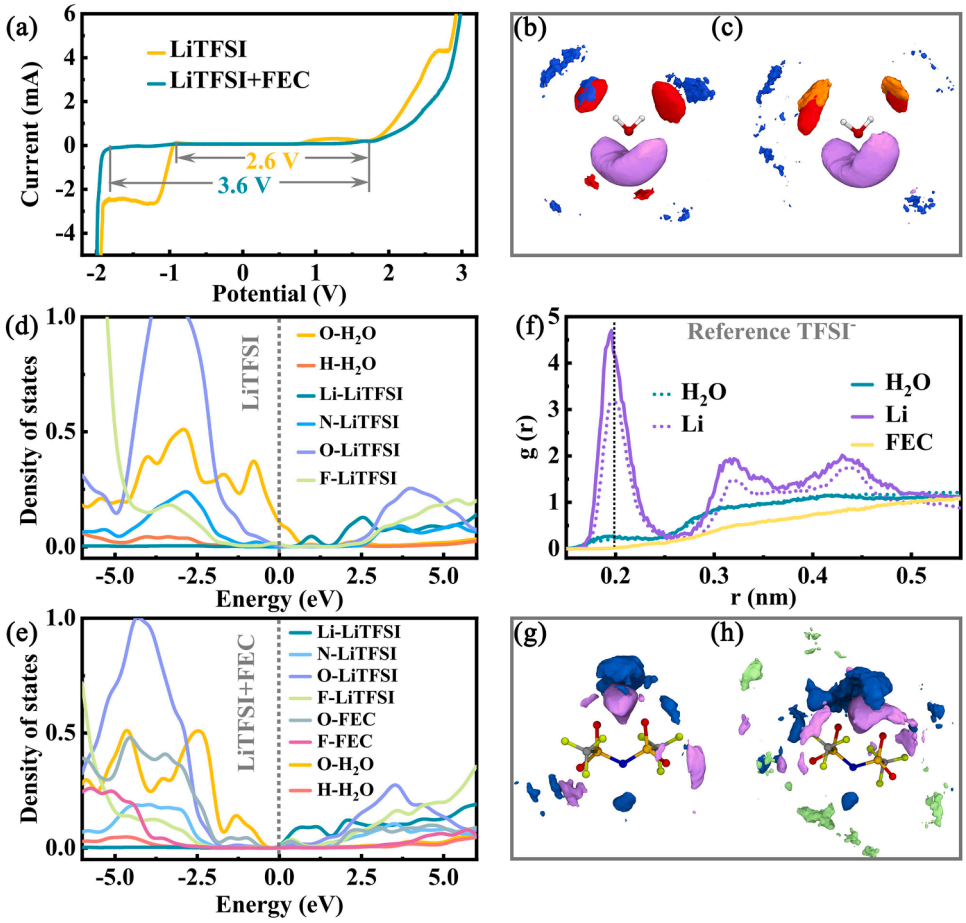

Fig. 1. Electrolyte electrochemical performance and structural evolution. (a) Linear sweep voltammetry (LSV) test curves for platinum sheet electrode in LiTFSI and FEC-added electrolytes. Saturated calomel electrode was used as reference electrode. (b) and (c) Spatial distribution functions (SDF) of water molecules. Purple, red, and blue are used to represent Li^+, O and N in $TFSI^-$, respectively, and orange is used to represent O in FEC. (d) and (e) The density of states (DOS) patterns for pristine and FEC-added electrolytes. (f) The radial distribution function (RDF) for both electrolytes. (g) and (h) SDF of $TFSI^-$ in pristine and FEC-added electrolyte, respectively. Purple, blue and green are used to represent Li^+, H_2O and FEC, respectively.

Table 1
The hydrogen bond density in LiTFSI and FEC-added electrolyte.

Acceptor[a]	H_2O:O [nm^{-3}][b]	LiTFSI:F [nm^{-3}]	LiTFSI:N [nm^{-3}]	LiTFSI:O [nm^{-3}]	FEC:O [nm^{-3}]	Total [nm^{-3}]
LiTFSI	3.51	2.33	0.69	4.96	0	11.50
FEC-added	1.70	0.69	0.24	2.32	1.23	6.18

[a] The donors are O of H_2O during the formation of the hydrogen bond process. The acceptors are O form H_2O, and F, N, O in LiTFSI and O in FEC.
[b] Hydrogen bond density unit is nm^{-3}.

effectively improve the discharge specific capacity of the graphite cathode. CV tests were performed on both electrolytes, using graphite as a cathode (Fig. 3b). A distinct cathodic peak at 1.78 V and two additional anodic peaks indicate the processes of the $TFSI^-$ anions intercalation/deintercalation into the graphite cathode [25]. The structural changes of graphite during charging and discharging were analyzed using XRD in the FEC-added electrolyte (Fig. 3c and Fig. 3d). The (002) peaks of graphite shifted right during charging and gradually returned to lower angles during the discharge process. These changes were caused by the ion intercalation of the graphite [26,27]. However, the (002) peak did not return to its original position during the first charge-discharge cycle, indicating that the intercalated $TFSI^-$ was not entirely removed from the graphite during the discharge process. The first cycle CV curve differed from the second and third cycles (Fig. S5) in FEC-added electrolyte. The coulomb efficiency (C.E.) of the first cycle was only 66 %, whereas the C.E. of the second cycle increased to 87 % (Fig. S6). This means that the remaining $TFSI^-$ ions in the graphite play a supporting role in the graphite layer and promoting the subsequent $TFSI^-$ ion intercalated into the graphite. The graphite structure underwent changes resembling those observed in the LiTFSI electrolyte (Fig. S7). And the first cycle CV and GCD curve differed from the second curve (Fig. S8 and Fig. S9). Interestingly, it can be observed from the CV curves that the polarization of the graphite cathode decreases in FEC-added electrolyte. The electron conduction of the graphite is invariant, while the ions are transported in the same way in the both electrolytes, so the decrease in polarization is mainly due to the accelerated electrochemical reaction rate on the graphite surface. Then XPS was used to analyze the surface of graphite cathode with full charging. The results of Li 1 s pattern showed that the content of Li on the graphite surface decreased after FEC was added, and the atomic percentage (At%) decreased from 1.31 % to 0.36 % (Fig. 3e). The F' At% is also reduced from 12.06 % to 6.58 %. The peak at 685.7 eV in the F 1 s pattern belongs to LiF (Fig. 3f and Fig. S10) [28]. It shows that CEI containing LiF is formed on the surface of graphite cathode during the charging. This phenomenon of LiTFSI decomposition at higher potential has been confirmed in LSV curves (Fig. 1a). The characteristic peak at 689 eV represents the LiTFSI salts and/or decomposition products of LiTFSI [29]. The inclusion of FEC reduces the presence of the electron and ion insulator LiF on the electrode surface. XPS proved that the addition of FEC could inhibit the generation of CEI. The activation energies of the graphite cathode in the both electrolytes are 28.279 and 16.893 kJ mol^{-1}, respectively, based on electrochemical

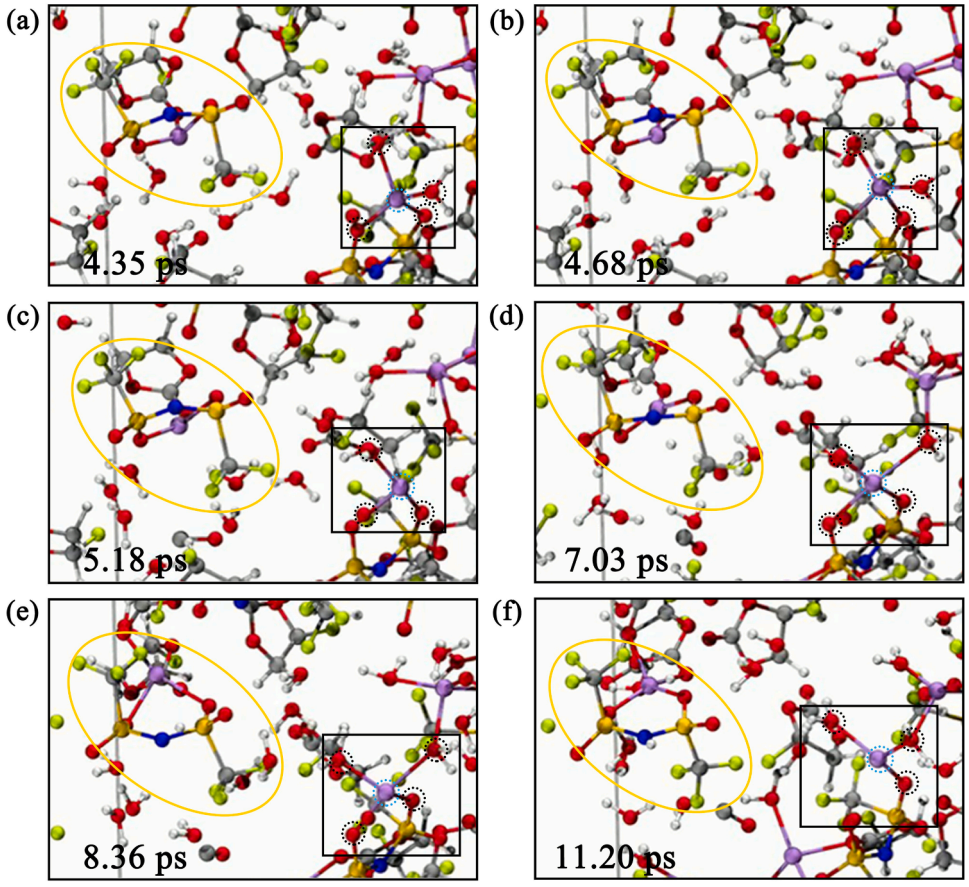

Fig. 2. Ion transport process in FEC-added electrolyte. (a-f) Images of the primary solvation sheath and surrounding chemical environment of ions at different times.

impedance spectroscopy and Formula S1 (Fig. 3g and Fig. S11-S12). The results show that the decrease of CEI is conducive to the $TFSI^-$ intercalation reaction using fewer transition state energy. The Raman imaging and secondary electron microscopy tests were carried out to investigate the surface state of graphite cathode in LiTFSI and FEC-added electrolytes. Fig. 3h-j depicts the test results of the pristine graphite, fully charged graphite in the LiTFSI and FEC-added electrolyte. The Raman mapping can be obtained by fitting different curves in the rectangular region. A brighter color indicates a larger I_g/I_d value. There are more bright yellow colors on the original graphite electrode (value of I_g/I_d is mainly concentrated in 4.5) and the color distribution is relatively uniform on the enlarged image [30–32]. The Raman mapping becomes dim when the graphite is fully charged in the pristine electrolyte, indicating that the value of I_g/I_d is decrease (I_g/I_d value mainly concentrated in 3.25). In addition, the color distribution of Raman mapping is not uniform, and the color on the top is gloomy and the bottom is brighter. It means that the formation of CEI on graphite surface is uneven distribution and defects increase. However, in FEC-added electrolyte, the color distribution of Raman mapping is uniform and the brighter (I_g/I_d value mainly concentrated in 3.5) compared to pristine electrolyte. Therefore, the addition of FEC makes the CEI on the graphite surface more uniform.

HRTEM is intuitive way to prove the impact of FEC on CEI. In the pristine electrolyte, there is a thicker CEI due to the presence of amorphous region on the graphite edge (Fig. 4a), but it becomes light and homogeneous in the FEC-added electrolyte (Fig. 4b). This is consistent with the results of Raman, demonstrating that FEC optimized electrolyte can inhibit the formation of CEI films during charging. At the same time, the (002) lattice plane of graphite has more defects in the FEC-added electrolyte compared with the pristine electrolyte. This indicates that relatively uniform and light CEI is beneficial to improve more $TFSI^-$ ions intercalated into the graphite layers, and resulting in more defects on the (002) lattice plane. The TOF-SIMS test tracked the distribution of the Li element, as shown in Fig. 4c and d. The addition of FEC significantly reduced the content of Li element on the surface of graphite (Top plane). This is consistent with the results of XPS. In the direction perpendicular to the graphite surface (Front plane), the Li element mainly exists within the depth range of 0 ~ 1.2 frames in the pristine electrolyte, while a trace amount of Li element is found in the FEC-added electrolyte. It further illustrated that the addition of FEC inhibits the formation of surface CEI. During charging, $TFSI^-$ ions migrate from the electrolyte to the graphite electrode, and some Li^+ ions are also present on the graphite surface due to solvation. The solvated $TFSI^-$ ions decompose to produce LiF, which in turn forms a thick and irregular CEI films on the graphite surface, preventing $TFSI^-$ ions rapidly intercalated into graphite cathode at a higher potential (Fig. 4e). Therefore, the whole graphite electrode has a large activation energy and polarization effect, and the final discharge capacity is only 22 mAh g^{-1}. In the FEC-added electrolyte, the activity of F atom in $TFSI^-$ is reduced due to the addition of FEC. In addition, FEC tends to be encapsulated outside water and Li^+ ions to form a solvation structure. FEC plays a protective role in the solvation structure of $TFSI^-$ and inhibits the decomposition of $TFSI^-$ due to its oxidation resistance, thus forming a filmy and uniform CEI film at higher potentials. This facilitates $TFSI^-$ ions from the electrolyte to be quickly intercalated into the graphite cathode (Fig. 4f), so that graphite cathode has a higher specific discharge capacity (47 mAh g^{-1}) and a lower polarization effect. Furthermore, using TOF-SIMS to track the F element on the graphite surface (Top plane) and perpendicular to graphite surface (Front plane). The content of F element on the graphite surface in FEC-added electrolyte (Fig. 4j) is significantly larger than that

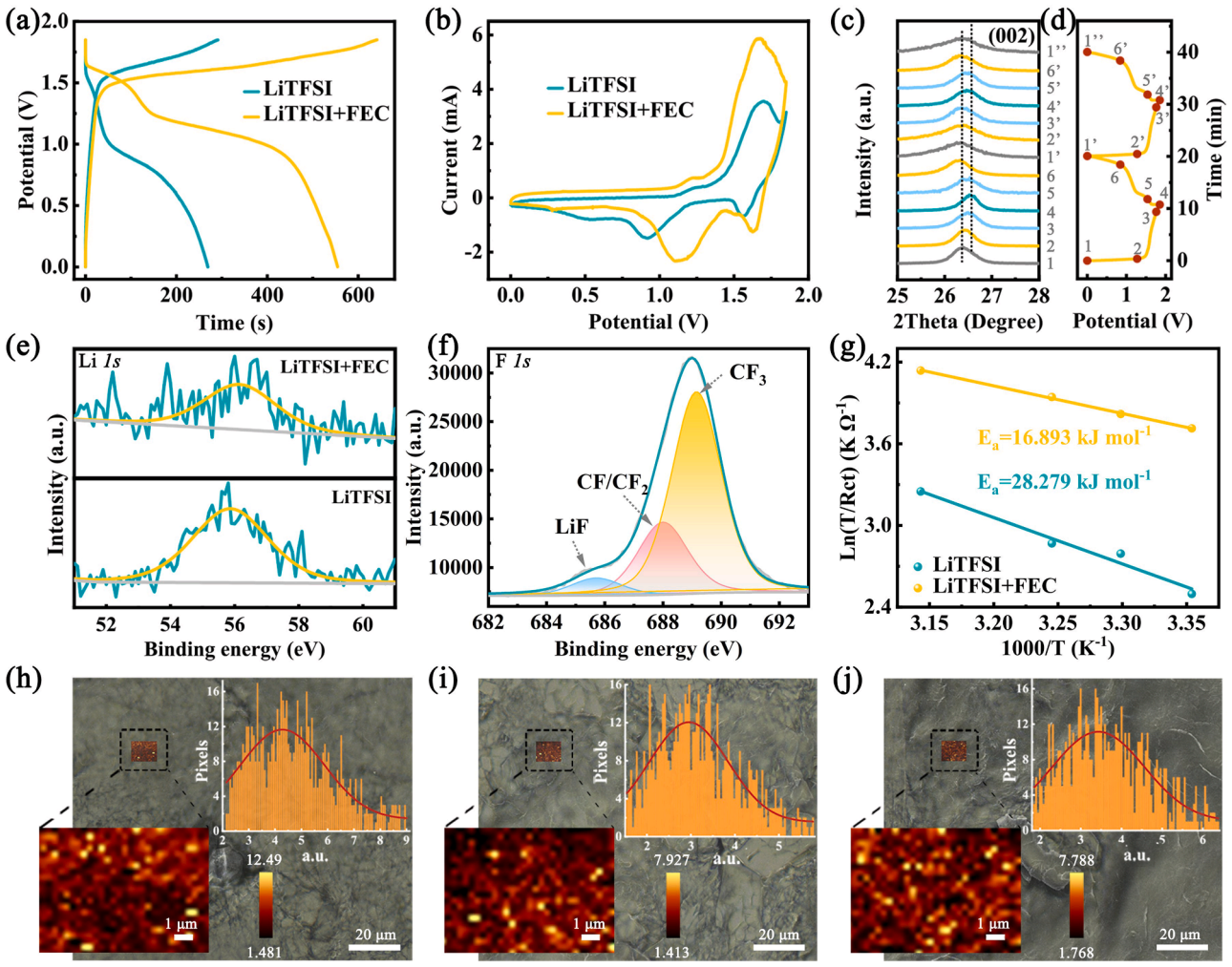

Fig. 3. Electrochemical performance and structural characterization of graphite cathode. (a) Galvanostatic charge discharge (GCD) profiles of graphite. (b) Cyclic voltammetry (CV) curves of $TFSI^-$ intercalation into graphite cathode at 1.0 mV s^{-1}. (c) *In-situ* XRD analysis of graphite structure in FEC-added electrolyte. (d) Sampling sites in the GCD curve. (e) X-ray photoelectron spectroscopy (XPS) of Li 1 s. (f) XPS curves of F 1 s for graphite cathode in FEC-added electrolyte. (g) Activation energy of $TFSI^-$ intercalation graphite based on the electrochemical impedance spectroscopy tests. (h-j) Raman imaging and secondary electron microscopy images of pristine graphite, fully charged graphite in LiTFSI and FEC-added electrolytes. Insets depict the distribution of Ig/Id values. The region of Raman analysis is enlarged and obtained by fitting characteristic spectral lines.

of pristine electrolyte (Fig. 4g). This is due to the fact that in addition to the $TFSI^-$ ions and CEI providing the F element in the FEC-added electrolyte, FEC also provides the F element. Combined with the SEM images of the tested area (Fig. 4g and Fig. 4i / Fig. 4j and Fig. 4l), which the F element is more likely to accumulate at the edges of graphite or in areas with large defects, while only a small amount of F element can be detected in relatively flat areas. This result implies that CEI are more likely to form at graphite defects or edges. In addition, an obvious F signal was detected within 1 ~ 1.2 frames on front in the pristine electrolyte, which is consistent with the detection results structure of Li element, and both belong to the CEI films signals (Fig. 4h). There are no obvious signals of F element with the increase of ion beam cutting depth. However, the F element signals can be detected, in the FEC electrolyte, with increasing ion beam cutting depth (Fig. 4k). This once again proves that the reduction of surface CEI film thickness is conducive to $TFSI^-$ ions intercalated into graphite to form GIC.

ATR infrared spectroscopy was used to analyze structure transformation of $TFSI^-$ during charge and discharge process in pristine and FEC-added electrolytes, as shown in Fig. 5a and Fig. 5b, respectively. The absorption peaks at 1348, 1198, 1140 and 1061 cm^{-1} positions belong to ν_aSO_2, ν_aCF_3, ν_sSO_2 and ν_aSNS, respectively [33]. In the LiTFSI electrolyte, the positions of the absorption peaks did not shift; however, their intensity increased or decreased during the charging and discharging process due to the influx of $TFSI^-$. Conversely, in the FEC-added electrolyte, these peaks exhibited red- and blue-shifting during the charging and discharging process. This phenomenon indicated the chemical state of $TFSI^-$ ions have changed, due to the strong interaction between $TFSI^-$ and graphite, modification of the charge distribution and force constant of the chemical bond. Subsequently, SXES was used to determine the electronic structure of the graphite (Fig. 4c and Fig. 4d). During charging, the C-K_α peak position shifted toward lower energy, indicating electron loss from the graphite. The larger ΔE (–0.16 eV) in the FEC-added electrolyte signified more intensively interaction between the $TFSI^-$ ions and the graphite, so the whole cathode lose more electrons to the outward circuit. However, during the discharge process, the peak position returned to its original position, indicating a reversible process. This finding aligned with the XRD results. In addition, the ATR infrared spectra of the both electrolytes under full charge were compared (Fig. S13). The absorption peak strength is larger in FEC-added electrolyte. These phenomena together indicate that $TFSI^-$ ions are more easily intercaleted into graphite electrodes in FEC-added electrolyte. The electrochemical method was used to further characterize the graphite cathode. The CV tests results indicated that the intercalation/deintercalation peaks of $TFSI^-$ retained their original

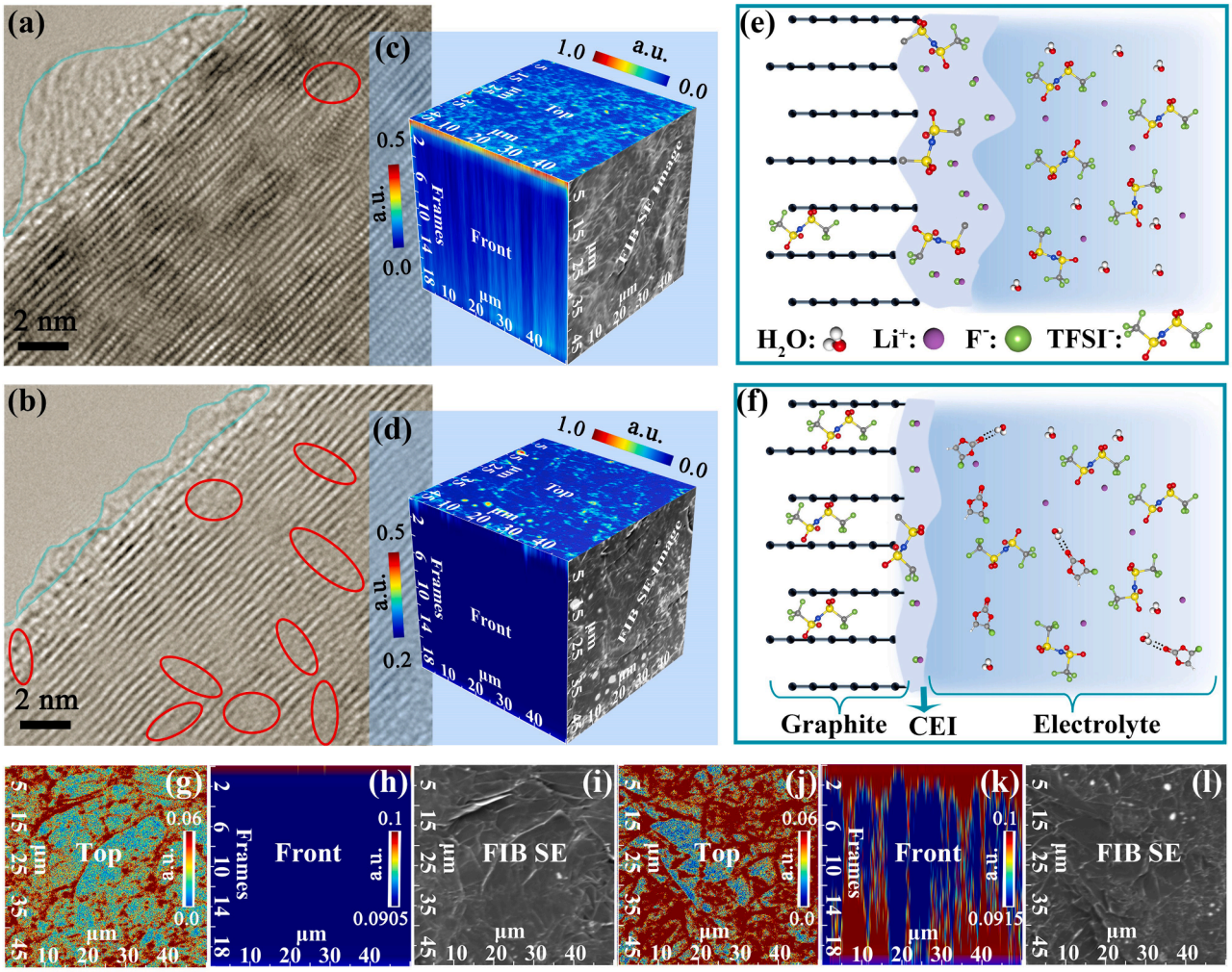

Fig. 4. Structural characterization for graphite cathode. (a) and (b) High resolution transmission electron microscopy (HRTEM) images of fully charged graphite in pristine and FEC-added electrolytes, respectively. (c) and (d) Time of flight secondary ion mass spectrometry (TOF-SIMS) pattern of Li element on graphite in pristine and FEC-added electrolytes. The plane of Top and Front are graphite surface and perpendicular to graphite surface (The scale of depth is frames), respectively. (e) and (f) Schematic illustration of $TFSI^-$ ions intercalated into graphite cathode in pristine and FEC-added electrolytes. (g) and (h) TOF-SIMS pattern of F element on the graphite surface (Top) and perpendicular to graphite surface (Front) in pristine electrolyte. (i) Scanning electron microscopy (SEM) image corresponding to the TOF-SIMS test area in pristine electrolyte. (j) and (k) TOF-SIMS pattern of F element on the graphite surface (Top) and perpendicular to graphite surface (Front) in FEC-added electrolyte. (l) SEM image corresponding to the TOF-SIMS test area in FEC-added electrolyte.

shapes as the sweep rate increased in FEC-added and pristine electrolyte (Fig. 5e and Fig. S14). This suggested that the $TFSI^-$ intercalated in graphite had good rate capability. The b values of Peak1, Peak2 and Peak3 were obtained using Formula S2. The b values of Peak1, Peak2 and Peak3 are 0.72, 0.72 and 0.84, respectively, in FEC-added electrolyte. But the b values of Peak 1, Peak 2 and Peak 3 in LiTFS electrolyte are 0.81, 0.93 and 0.82, respectively (Fig. 5f and Fig. S15). FEC caused a shift from surface-controlled current to diffusion-controlled current. This implies that the bulk phase reaction is dominant in the FEC-added electrolyte. The diffusion coefficient (D) was obtained using GITT and Formula S3 (Fig. 5g and Fig. S16-S17). The D of the FEC-added electrolyte exceeded that of the LiTFSI electrolyte, indicating graphite had a faster kinetic process in the FEC-added electrolyte, due to that $TFSI^-$ ions migration was enhanced by inhibiting CEI production.

2.3. Electrochemical characterization of full cell

To demonstrate the practical applicability of the FEC-added electrolyte, a dual-ion battery was assembled with graphite and PTCDI as the cathode and anode electrodes, respectively. During the charging process, $TFSI^-$ and Li^+ ions migrate to the cathode and the anode, respectively (Fig. 6a). The capacity ratio of the negative to positive electrode (N/P ratio) is 0.88, as shown in Table S2. The electrochemical window of this battery reached 2.55 V (Fig. S18). The first cycle discharge capacity was 26 mAh g^{-1}, and the C.E. was 58%, in FEC-added electrolyte. The capacity of the second and third cycles remained consistent at 26 mAh g^{-1}, but the C.E. increased to 76 % (Fig. 6b). The lower C.E. in the first cycle may have resulted from the formation of SEI/CEI film at the anode/cathode and incomplete removal of $TFSI^-$ ions from the graphite at the cathode. The CV curves indicated a gradual increase in cathode/anode peaks with the sweep rate, whereas the peak position remained mostly unchanged. This verified the battery's strong rate capability and slight polarization (Fig. 6c). The energy densities, recorded to be 66, 56, 52, 47, 44 and 40 Wh kg^{-1} at 128, 255, 383, 510, 638 and 765 W kg^{-1}, respectively, had an average C.E. of approximately 90 % (Fig. 6d). However, the discharge capacity of the dual-ion battery composed of LiTFSI electrolyte is only 15 mAh g^{-1} at 50 mA g^{-1}. In addition, comparing the CV curves, it can be seen that the potential difference between the oxidation and the reduction peak of the full cell with FEC-added electrolyte is mild, which proves that the polarization effect is slight (inset of Fig. 6e). This result is consistent with the performance of graphite cathode, indicating that the FEC' positive impact

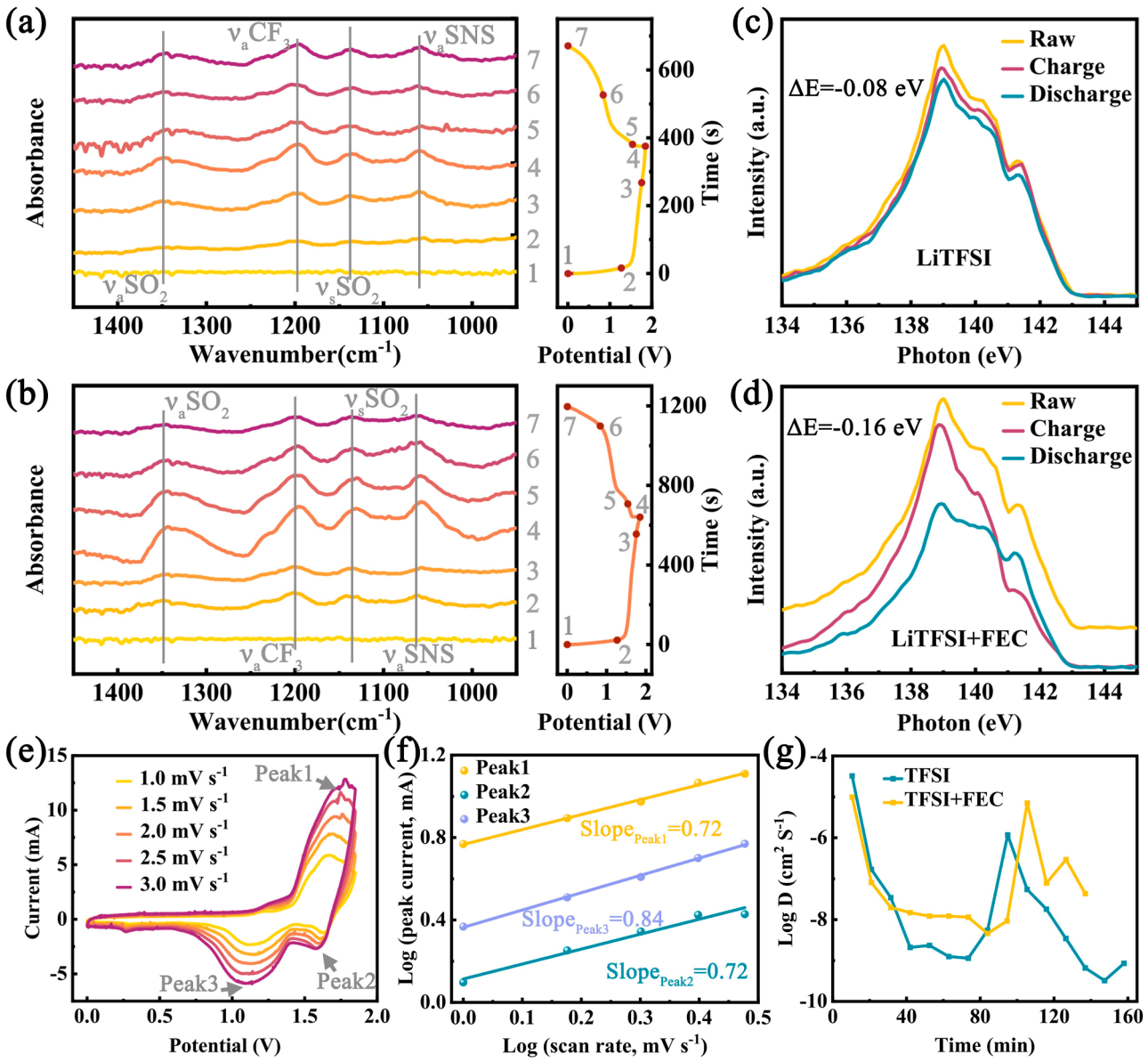

Fig. 5. Structural characterization of graphite cathode. (a) and (b) ATR infrared spectroscopy of $TFSI^-$ at different potentials in LiTFSI and FEC-added electrolytes. (c) and (d) Soft X-ray emission spectrometer (SXES) of graphite in both electrolytes. (e) CV curves of graphite at different scan rates in FEC-added electrolyte. (f) Linearly fitted log (i) versus log (v) plot at peak current for graphite in FEC-added electrolyte. (g) Diffusion coefficient based on galvanostatic intermittent titration technique (GITT) test.

remains effective even when constructing a full cell. After 1000 cycles, the battery attained an energy density of 90 % and experienced minimal attenuation in C.E. relative to the second cycle, when using the FEC-added electrolyte, exhibited optimized cycle stability (Fig. S19). Using FEC to optimize LiTFSI aqueous electrolyte compared with other optimization methods, such as using high concentration or double salt as electrolyte, can achieve higher discharge capacity at higher current density and has a considerable price advantage (Fig. 6f).

3. Conclusion

FEC, used as an additive and diluent, can both enlarge the potential window of LiTFSI aqueous electrolyte and reduce the electrolyte concentration. Uniform and light CEI can be established benefited from the change of $TFSI^-$' solvation structure. This is due to the fact that FEC with high oxidation resistance participates in the solvation structure of $TFSI^-$, which protects $TFSI^-$ ions from continuous decomposition at high potential. Thus, the graphite electrode achieves an approximately doubled discharge capacity with 47 mAh g^{-1} in contrast to the unoptimized electrolyte. In addition, this CEI is more likely to form at the site of surface defects. This work fills a gap in the study of the effect of anion solvation structure on CEI structure. Ultimately, we successfully assembled a dual-ion battery with a potential window of 2.55 V. Under a power density of 128 W kg^{-1}, this battery achieved an energy density of up to 66 Wh kg^{-1}.

4. Experimental methods

4.1. Preparation of electrodes and electrolytes

Commercial graphite paper directly as cathode. The $C_{24}H_{10}N_2O_4$ (PTCDI), super P and PVDF were prepared as electrode slurry in the mass ratio of 7 : 1.5 : 1.5, using N-Methylpyrrolidone as solvent. The prepared electrode slurry was coated on the graphite paper substrate. The dried

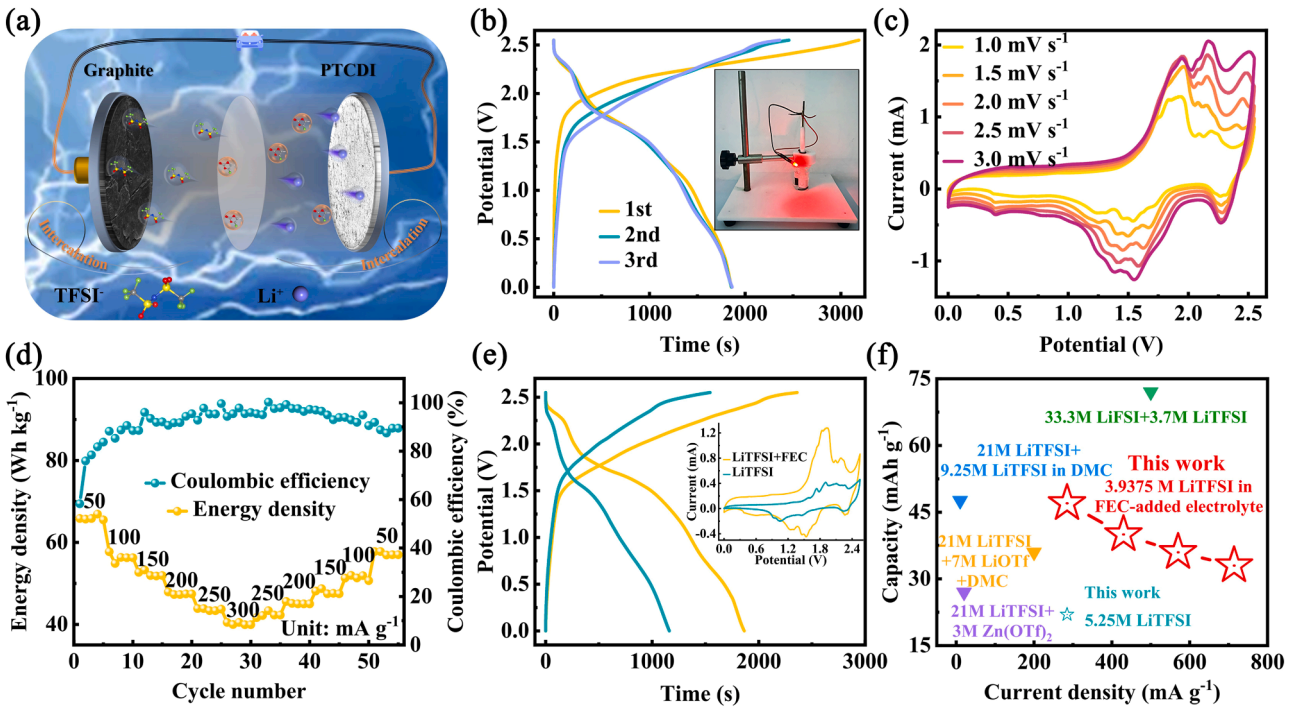

Fig. 6. Electrochemical characterization of full cell using graphite and PTCDI as cathode and anode, respectively. (a) Structural diagram of full cell. (b) GCD profiles of first three cycles of full cell with FEC-added electrolyte at 50 mA g^{-1} current density. (c) CV curves of full cell with FEC-added electrolyte at different scan rates. (d) Rate capability and corresponding coulomb efficiency of full cell with FEC-added electrolyte. (e) GCD profiles of full cell in pristine and FEC-added electrolyte. Inset is comparison of the CV curves of full cell in the two electrolytes. (f) Graphite cathode performance comparison in aqueous electrolytes [34–37].

electrode sheet is used as anode. The 5.25 M LiTFSI electrolyte was obtained by dissolving 18.08667 g of LiTFSI in 3 ml deionized water, labeled as LiTFSI. Subsequently 4 ml FEC was added to the prepared LiTFSI electrolyte to obtain the optimized electrolyte noted as FEC-added electrolyte. Now, the FEC-added electrolyte concentration is reduced to 3.9375 M.

4.2. Characterization of electrodes and electrolyte

Structural of LiTFSI and FEC-added electrolyte was analyzed using ATR infrared spectroscopy and Raman. The LSV tests were also performed with CHI660E electrochemical workstation. The contact angles of the two electrolytes were tested by Krüss DSA 30 equipment. Structural analysis of graphite cathode using powder X-ray diffraction (XRD, a Bruker D8 Advance diffractometer with Cu Kα radiation) and *in-situ* X-ray diffraction lithium-ion battery equipment (The 2theta is 10° ~ 90°; The diameter and thickness are 50 mm and 14 mm, respectively) from Beijing Scistar Technology Co. Ltd, TEM (JEM 2100F) and SXES (SS-94000SXES in JSM-7900F). Raman and TOF-SIMS were performed using WITec Alpha 300 R in TESCAN S9000G. The chemical state of the electrode surface was analyzed using ATR infrared spectroscopy and XPS. Electrochemical characterization using CHI660E electrochemical workstation. platinum sheet is used as the working electrode for LSV testing. The electrochemical performance of the single electrode was tested using a three-electrode system. The saturated calomel electrode (SCE) and the platinum sheet were used as the reference electrode and counter electrode, respectively.

4.3. Computational methods

The Ab initio molecular dynamics (AIMD) simulations were carried out using the CP2K software package with Quickstep method for both electrolytes [38]. Using the Perdew-Burke-Ernzerhof (PBE) density functional, based on the generalized gradient approximation (GGA), along with Grimme's dispersion correction was adopted [39]. The DZVP-MOLOPT atomic basis set [40] with Goedecker-Teter-Hutter pseudopotentials [41] was used to describe the wave function. The Brillouin zone was sampled at the Γ-point. The spatial density distribution was calculated by Travis [42]. The radial distribution function was calculated by gromacs rdf [43]. The PDOS was calculated by Multiwfn program [44]. The visualization of the structures is accomplished using the VMD program [45]. The H-bond analysis was performed using MD Analysis library [46]. The simulation box of LITFSI electrolyte contains 29 waters, and 11 LiTFSI (263 atoms). The simulation box of FEC-added electrolyte contains 29 waters, 11 LiTFSI and 11 FEC (381 atoms). To obtain the densities of these two systems, first, simulation within an isothermal-isobaric ensemble (NPT) for 50 ps with a 1 fs timestep was applied in Gromacs. Then, the canonical ensemble (NVT) in CP2K was used to perform another 50 ps simulation with a 400 Ry cutoff for trajectory analysis. To evaluate the desolvation energy, the proper solvation shell was built according to coordinate number and calculated at PBE0-D3BJ/def2-SVP level with acetone as solvent in PCM solvation model [47], utilizing the ORCA 5.0.4 program.

CRediT authorship contribution statement

Ying Zheng: Writing – original draft, Resources, Methodology, Investigation, Formal analysis, Data curation, Conceptualization. **Wei Zhang:** Writing – review & editing, Supervision, Project administration, Funding acquisition, Conceptualization. **Fuxi Liu:** Investigation. **Qing Liang:** Investigation. **Wenwen Li:** Investigation. **Xinyan Zhou:** Investigation. **Nailin Yue:** Investigation. **Weitao Zheng:** Writing – review & editing, Supervision, Project administration, Funding acquisition, Conceptualization.

Declaration of competing interest

The authors declare that they have no known competing financial interests or personal relationships that could have appeared to influence the work reported in this paper.

Acknowledgements

This research was supported by the National Natural Science Foundation of China (51932003 and 52272209). The authors would also like to thank Shiyanjia Lab (www.Shiyanjia.com) for the theoretical simulations. The authors express their sincere thanks to Prof. Heng Zhang and Prof. Qiang Zhang for their stimulating discussions.

Data availability

Data will be made available on request.

Supplementary materials

Supplementary material associated with this article can be found, in the online version, at doi:10.1016/j.ensm.2024.103326.

References

[1] L. Suo, O. Borodin, T. Gao, M. Olguin, J. Ho, X. Fan, C. Luo, C. Wang, K. Xu, "Water-in-salt" electrolyte enables high-voltage aqueous lithium-ion chemistries, Science 350 (2015) 6263.
[2] X. Bogle, R. Vazquez, S. Greenbaum, A. Cresce, K. Xu, Li^{+}-solvent interaction in Nonaqueous carbonate electrolytes with ^{17}O NMR, J. Phys. Chem. Lett. 4 (2013) 1664–1668.
[3] Z. Huang, Y. Hou, T. Wang, Y. Zhao, G. Liang, X. Li, Y. Guo, Q. Yang, Z. Chen, Q. Li, L. Ma, J. Fan, C. Zhi, Manipulating anion intercalation enables a high-voltage aqueous dual ion battery, Nat. Commun. 12 (2021) 3106.
[4] L. Jiang, Y. Lu, C. Zhao, L. Liu, J. Zhang, Q. Zhang, X. Shen, J. Zhao, X. Yu, H. Li, X. Huang, L. Chen, Y.S. Hu, Building aqueous K-ion batteries for energy storage, Nat. Energy 4 (2019) 495–503.
[5] X. Bu, L. Su, Q. Dou, S. Lei, X.X. Bu, L. Su, Q. Dou, S. Lei, X. Yan, A low-cost "water-in-salt" electrolyte for a 2.3 V high-rate carbon-based supercapacitor, J. Mater. Chem. A 7 (2019) 7541–7547.
[6] X. Wu, Y. Xu, C. Zhang, D.P. Leonard, A. Markir, J. Lu, X. Ji, Reverse Dual-Ion Battery via a $ZnCl_2$ Water-in-Salt electrolyte, J. Am. Chem. Soc. 141 (2019) 6338–6344.
[7] J. Zheng, G. Tan, P. Shan, T. Liu, J. Hu, Y. Feng, L. Yang, M. Zhang, Z. Chen, Y. Lin, J. Lu, J.C. Neuefeind, Y. Ren, K. Amine, L.W. Wang, K. Xu, F. Pan, Understanding thermodynamic and kinetic contributions in expanding the stability window of aqueous electrolytes, Chem 4 (2018) 2872–2882.
[8] M.R. Lukatskaya, J.I. Feldblyum, D.G. Mackanic, F. Lissel, D.L. Michels, Y. Cui, Z. Bao, Concentrated mixed cation acetate "water-in-salt" solutions as green and low-cost high voltage electrolytes for aqueous batteries, Energy Environ. Sci. 11 (2018) 2876–2883.
[9] K.I. Kim, Q. Guo, L. Tang, L. Zhu, C. Pan, C.H. Chang, J. Razink, M.M. Lerner, C. Fang, X. Ji, Reversible insertion of Mg-Cl superhalides in graphite as a cathode for aqueous dual-ion batteries, Angew. Chem. Int. Ed. 59 (2020) 19924–19928.
[10] H. Jia, J.M. Kim, P. Gao, Y. Xu, M.H. Engelhard, B.E. Matthews, C. Wang, W. Xu, A Systematic Study on the Effects of Solvating Solvents and Additives in Localized High-Concentration Electrolytes over Electrochemical Performance of Lithium-Ion Batteries, Angew. Chem. Int. Ed. 62 (2023) e202218005.
[11] C. Yan, L.L. Jiang, Y.X. Yao, Y. Lu, J.Q. Huang, Q. Zhang, Nucleation and growth mechanism of anion-derived solid electrolyte interphase in rechargeable batteries, Angew. Chem. Int. Ed. 60 (2021) 8521–8525.
[12] S. Lin, H. Hua, P. Lai, J. Zhao, A Multifunctional Dual-Salt Localized High-Concentration Electrolyte for Fast Dynamic High-Voltage Lithium Battery in Wide Temperature Range, Adv. Energy Mater. 11 (2021) 2101775.
[13] Z. Huang, T. Wang, X. Li, H. Cui, G. Liang, Q. Yang, Z. Chen, A. Chen, Y. Guo, J. Fan, C. Zhi, Small-Dipole-Molecule-containing electrolytes for high-voltage aqueous rechargeable batteries, Adv. Mater 34 (2022) e2106180.
[14] P. Jaumaux, X. Yang, B. Zhang, J. Safaei, X. Tang, D. Zhou, C. Wang, G. Wang, Localized "water-In-Salt" electrolyte for aqueous lithium-ion batteries, Angew. Chem. Int. Ed. 60 (2021) e1800533.
[15] G. Wang, M. Yu, J. Wang, D. Li, D. Tan, M. Loffler, X. Zhuang, K. Mullen, X. Feng, Self-Activating, Capacitive Anion Intercalation Enables High-Power Graphite Cathodes, Adv. Mater. 30 (2018) e1800533.
[16] Y. Wei, B. Tang, X. Liang, F. Zhang, Y. Tang, An Ultrahigh-mass-loading integrated free-standing functional all-carbon positive electrode prepared using an architecture tailoring strategy for high-energy-density dual-ion batteries, Adv. Mater. 35 (2023) 2302086.
[17] C. Han, H. Wang, Z. Wang, X. Ou, Y. Tang, Solvation structure modulation of high-voltage electrolyte for high-performance K-based dual-graphite battery, Adv. Mater. 35 (2023) 2300917.
[18] Z. Yu, P.E. Rudnicki, Z. Zhang, Z. Huang, H. Celik, S.T. Oyakhire, Y. Chen, X. Kong, S.C. Kim, X. Xiao, H. Wang, Y. Zheng, G.A. Kamat, M.S. Kim, S.F. Bent, J. Qin, Y. Cui, Z. Bao, Rational solvent molecule tuning for high-performance lithium metal battery electrolytes, Nat. Energy 7 (2022) 94–106.
[19] Y. Yamada, J. Wang, S. Ko, E. Watanabe, A. Yamada, Advances and issues in developing salt-concentrated battery electrolytes, Nat. Energy 4 (2019) 269–280.
[20] L. Qin, N. Xiao, J. Zheng, Y. Lei, D. Zhai, Y. Wu, Localized high-concentration electrolytes boost potassium storage in high-loading graphite, Adv. Energy Mater 9 (2019) 1902618.
[21] Y. Hu, L. Fan, A.M. Rao, W. Yu, C. Zhuoma, Y. Feng, Z. Qin, J. Zhou, B. Lu, Cyclic-anion salt for high-voltage stable potassium-metal batteries, Natl. Sci. Rev. 9 (2022) 134.
[22] J. Li, Y. Hu, H. Xie, J. Peng, L. Fan, J. Zhou, B. Lu, Weak Cation-solvent interactions in ether-based electrolytes stabilizing potassium-ion batteries, Angew. Chem. Int. Ed. 61 (2022) e202208291.
[23] L. Fan, H. Xie, Y. Hu, Z. Caixiang, A.M. Rao, J. Zhou, B. Lu, A tailored electrolyte for safe and durable potassium ion batteries, Energy Environ. Sci. 16 (2023) 305–315.
[24] X. Ma, H. Fu, J. Shen, D. Zhang, J. Zhou, C. Tong, A.M. Rao, J. Zhou, L. Fan, B. Lu, Green ether electrolytes for sustainable high-voltage potassium ion batteries, Angew. Chem. Int. Ed 62 (2023) e202312973.
[25] X. Zhou, Q. Liu, C. Jiang, B. Ji, X. Ji, Y. Tang, H.M. Cheng, Strategies towards Low-Cost Dual-Ion batteries with high performance, Angew. Chem. Int. Ed. 59 (2020) 3802–3832.
[26] Z. Zhou, N. Li, Y. Yang, H. Chen, S. Jiao, W.L. Song, D. Fang, Ultra-lightweight 3D carbon current collectors: constructing all-carbon electrodes for stable and high energy density dual-ion batteries, Adv. Energy Mater. 8 (2018) 1801439.
[27] M.C. Lin, M. Gong, B. Lu, Y. Wu, D.Y. Wang, M. Guan, M. Angell, C. Chen, J. Yang, B.J. Hwang, H. Dai, An ultrafast rechargeable aluminium-ion battery, Nature 520 (2015) 325–328.
[28] G.G. Eshetu, T. Diemant, S. Grugeon, R.J. Behm, S. Laruelle, M. Armand, S. Passerini, In-depth interfacial chemistry and reactivity focused investigation of lithium-imide- and lithium-imidazole-based electrolytes, ACS Appl. Mater. Interfaces 8 (2016) 16087–16100.
[29] P.M. Shanthi, P.J. Hanumantha, K. Ramalinga, B. Gattu, M.K. Datta, Sulfonic acid based complex framework materials (CFM): nanostructured polysulfide immobilization systems for rechargeable lithium–sulfur battery, J. Electrochem. Soc. 166 (2019) A1827–A1835.
[30] Y. Zheng, T. Deng, W. Zhang, W. Zheng, Optimizing the micropore-to-mesopore ratio of carbon-fiber-cloth creates record-high specific capacitance, J. Energy Chem. 47 (2020) 210–216.
[31] Y. Zheng, T. Deng, N. Yue, W. Zhang, X. Zhu, H. Yang, X. Chu, W. Zheng, Raman spectroscopy and correlative-Raman technology excel as an optimal stage for carbon-based electrode materials in electrochemical energy storage, J Raman Spectrosc 52 (2021) 2119–2130.
[32] L. Fan, Q. Liu, S. Chen, K. Lin, Z. Xu, B. Lu, Potassium-based dual ion battery with dual-graphite electrode, Small 13 (2017) 1701011.
[33] K. Kim, L. Kuhn, I.V. Alabugin, D.T. Hallinan, Hallinan, lithium salt dissociation in Diblock copolymer electrolyte using fourier transform infrared spectroscopy, Front. Energy Res. 8 (2020) 569442.
[34] J.M. Wrogemann, S. Künne, A. Heckmann, I.A. Rodríguez-Pérez, V. Siozios, B. Yan, J. Li, M. Winter, K. Beltrop, T. Placke, Development of safe and sustainable dual-ion batteries through hybrid Aqueous/Nonaqueous electrolytes, Adv. Energy Mater. 10 (2020) 1902709.
[35] H. Zhang, X. Liu, B. Qin, S. Passerini, Electrochemical intercalation of anions in graphite for high-voltage aqueous zinc battery, J. Power Sources 449 (2020) 227594.
[36] J. Zhu, Y. Xu, Y. Fu, D. Xiao, Y. Li, L. Liu, Y. Wang, Q. Zhang, J. Li, X. Yan, Hybrid Aqueous/Nonaqueous water-in-Bisalt electrolyte enables safe dual ion batteries, Small 16 (2020) e1905838.
[37] H. Li, T. Kurihara, D. Yang, M. Watanabe, T. Ishihara, A novel aqueous dual-ion battery using concentrated bisalt electrolyte, Energy Stor. Mater. 38 (2021) 454–461.
[38] T.D. Kuhne, M. Iannuzzi, M. Del Ben, V.V. Rybkin, P. Seewald, F. Stein, T. Laino, R. Z. Khaliullin, O. Schutt, F. Schiffmann, D. Golze, J. Wilhelm, S. Chulkov, M. H. Bani-Hashemian, V. Weber, U. Borstnik, M. Taillefumier, A.S. Jakobovits, A. Lazzaro, H. Pabst, T. Muller, R. Schade, M. Guidon, S. Andermatt, N. Holmberg, G.K. Schenter, A. Hehn, A. Bussy, F. Belleflamme, G. Tabacchi, A. Gloss, M. Lass, I. Bethune, C.J. Mundy, C. Plessl, M. Watkins, J. VandeVondele, M. Krack, J. Hutter, CP2K: an electronic structure and molecular dynamics software package - Quickstep: efficient and accurate electronic structure calculations, J. Chem. Phys. 152 (2020) 194103.
[39] S. Grimme, J. Antony, S. Ehrlich, H. Krieg, A consistent and accurate ab initio parametrization of density functional dispersion correction (DFT-D) for the 94 elements H-Pu, J. Chem. Phys. 132 (2010) 154104.
[40] J.V. Vondele, J. Hutter, Gaussian basis sets for accurate calculations on molecular systems in gas and condensed phases, J. Chem. Phys. 127 (2007) 114105.
[41] S. Goedecker, M. Teter, J. Hutter, Separable dual-space Gaussian pseudopotentials, Phys. Rev. B 54 (1996) 1703–1710.
[42] M. Brehm, M. Thomas, S. Gehrke, B. Kirchner, TRAVIS-A free analyzer for trajectories from molecular simulation, J. Chem. Phys. 152 (2020) 164105.
[43] M.J. Abraham, T. Murtola, R. Schulz, S. Páll, J.C. Smith, B. Hess, E. Lindahl, GROMACS: high performance molecular simulations through multi-level parallelism from laptops to supercomputers, SoftwareX 1-2 (2015) 19–25.
[44] T. Lu, F. Chen, Multiwfn: a multifunctional wavefunction analyzer, J Comput Chem 33 (2012) 580–592.

[45] W. Humphrey, A. Dalke, K. Schulten, VMD: visual molecular dynamics, J. Mol. Graphi. 14 (1996) 33–38.
[46] N.M. Agrawal, E.J. Denning, T.B. Woolf, O. Beckstein, MD Analysis: a toolkit for the analysis of molecular dynamics simulations, J Comput Chem 32 (2011) 2319–2327.
[47] G. Scalmani, M.J. Frisch, Continuous surface charge polarizable continuum models of solvation, J. Chem. Phys. 132 (2010) 114110.